Journal of Biomedical Optics 13(5), 054024 (September/October 2008)

Nonlinear optical microscopy of the bronchus

Shuangmu Zhuo
Jianxin Chen
Biying Yu
Xingshan Jiang
Teng Luo
Quangang Liu
Rong Chen
Shusen Xie
Fujian Normal University
Institute of Laser and Optoelectronics Technology
Fujian Provincial Key Laboratory for Photonics Technology
Key Laboratory of Optoelectronic Science
and Technology for Medicine
Ministry of Education
Fuzhou 350007, P. R. China

Abstract. Because of frequent exposure to carcinogens, the bronchus is prone to early pathologic alterations. The assessment of these early changes is of key significance in physiological studies and disease diagnosis of the bronchus. We utilize nonlinear optical microscopy (NLOM) to image mouse bronchial tissue based on intrinsic nonlinear optical contrast. Our results show that NLOM is effective for imaging the bronchial intact microstructural components, providing quantitative information about the biomorphology and biochemistry of tissue. Our findings also display that NLOM can provide a two-photon ratiometric redox fluorometry, based on mitochondrial signals and reduced pyridine nucleotide (NADH and NADPH) and oxidized flavoproteins (Fp) signals, to assess the metabolic state of the epithelial cells and chondrocytes. It was found that NLOM can offer a sensitive tool, based on the second-harmonic signal depth-dependent decay, to obtain quantitative information on the optical property of the stroma associated with normal and diseased tissue states. Our results suggest that with the advent of the clinical portability of typical nonlinear optical endoscopy, the NLOM technique has the potential to be applied *in vivo* to the clinical diagnosis and monitoring of bronchial disease.

[DOI: 10.1117/1.2982534]

Keywords: nonlinear optical microscopy (NLOM); bronchus; intrinsic nonlinear optical contrast.

Paper 07463RR received Nov. 12, 2007; revised manuscript received Apr. 8, 2008; accepted for publication May 14, 2008; published online Sep. 23, 2008.

1 Introduction

Because of frequent exposure to carcinogens, such as tobacco smoke components, the bronchus is prone to early pathologic alterations. During pathologic progression, a number of morphological and function changes have been observed, such as an increase in nuclear size and nuclear/cytoplasmic ratio, an increase in epithelial thickness, an increase in metabolic rate, changes in autofluorescence of biochemical markers, or alterations in extracellular matrix architecture.[1–3] In addition, hyaline cartilage is also damaged during the development of disease.[4]

So far, assessment of these early changes relied primarily on gross in section during an endoscopic procedure and pathologic examination of biopsy samples derived from the macroscopy. There have been enormous advances in understanding molecular mechanisms responsible for pathologic alterations; however, the destructive nature of these techniques makes the detection of these changes within intact tissue difficult.

High-resolution imaging utilizing intrinsic optical signals from microstructural components in intact bronchial tissue without the need for sectioning, preparation, or staining would allow an improved study of bronchus physiology with fewer artifacts. Such technology could aid in early detection of bronchial diseases.[3] Presently, clinical noninvasive techniques such as magnetic resonance imaging (MRI) and endobronchial ultrasound lack one resolution needed to distinguish complex structures of the bronchus, although the sensitivity and applicability of these techniques continue to improve and expand.[5,6] Fluorescence bronchoscopy remains a very useful, minimally invasive technique, but the technique is hampered by low specificity, which ranges from 25 to 50%.[7] Optical coherence tomography (OCT) provides full-thickness, high-resolution ($\sim 10\ \mu\text{m}$), cross-sectional images of the bronchus but lacks the ability to distinguish among biological constituents.[2] Laser scanning confocal microscopy (LSCM) provides a useful tool for biomedicine but has phototoxicity problems for imaging tissues because it uses an ultraviolet light source.[8] Nonlinear optical microscopy (NLOM) has several advantages over confocal microscopy because it uses a near-infrared light source, providing high-resolution images at increased imaging depths, minimal out-of-plane absorption, and inherent optical sectioning and providing a powerful tool for imaging live tissues.[8,9] More recently, with the advent of nonlinear optical microendoscopy,[10–12] the nonlinear optical imaging technique has been extended to *in vivo* applications. That fact further confirms the potential of the nonlinear optical imaging technique for the *in vivo* imaging in bronchial tissues.

NLOM is a nondestructive, laser scanning microscopy technique that renders images of living tissue with subcellular

---

Address all correspondence to Jianxin Chen, Key Laboratory of Optoelectronic Science and Technology for Medicine (Fujian Normal: Univ.), Ministry of Education, Fuzhou 35007, China; Tel: +86-591-22686078; Fax: +86-591-83465373; E-mail: chenjianxin@fjnu.edu.cn

1083-3668/2008/13(5)/054024/7/$25.00 © 2008 SPIE

resolution based on intrinsic optical contrast of biological tissues. Using backreflected experimental geometry, NLOM is suitable for the more practical case of thick, unstained living specimens. NLOM is very sensitive in defining cellular and extracellular structures as well as metabolic assessment.[13–22]

In this study, we used NLOM to image mouse bronchial tissue based on intrinsic nonlinear optical contrast.

2 Materials and Methods

2.1 *Specimen Preparation*

The bronchial tissues of five experimental mice were examined in this study. The fresh specimens were excised from living experimental mice, provided by the Animal Center of Fujian Medical University. First, they were rinsed briefly with phosphate buffered saline (PBS) solution (pH 7.4) to remove the residual blood on their surfaces. Then the bronchus were opened longitudinally and sandwiched between the microscope slide and a piece of the cover glass. Moreover, to avoid dehydration or shrinkage during the whole imaging process, a little PBS solution was dripped on the specimen. In this work, to keep tissues viable, the duration of the experiment was not more than 1 h.

2.2 *Nonlinear Optical Microscopy (NLOM)*

The nonlinear microscopy system used in this study has been described previously.[23] The source was a femtosecond Ti:sapphire laser (Coherent Mira 900-F). The excitation and emission light were coupled through an inverted microscope (Zeiss LSM 510 META) with a 63× oil-immersion objective (Zeiss, Plan-Apochromat, NA 1.4). Laser intensity attenuation was implemented using an acousto-optic modulator (AOM, Zeiss), and the polarization direction of the laser light is horizontal. Excitation wavelengths of 760 nm and 810 nm were used, and the average power was controlled at $P \leqslant 6$ mW. The beam of the laser was scanned in the focal plane by a galvanometer-driven optical scanner (Zeiss). A main dichroic beamsplitter (HFT KP685, Zeiss) was used to reflect the incident excitation laser source to the sample and direct the signals to the detector. Backward signals were detected with the META detector, which consists of a high-quality, reflective grating as a dispersive element and an optimized 32-channel photomultiplier tube (PMT) array capable of collecting different frequency ranges separated by 10.7 nm. The range of detection is from 377 to 716 nm. To get rid of the excitation light, an IR beam block filter (KP650, Zeiss) was placed in front of META detector. In this work, to change and record the focus position, an optional HRZ 200 fine-focusing stage (HRZ 200 stage, Zeiss) was used. The system has two imaging modes: channel mode and Lambda mode. The channel mode can achieve (TPEF), second-harmonic generation (SHG), and TPEF/SHG imaging, while the Lambda mode can carry out spectral imaging and obtain emission spectra of the region of interest within the spectral image by plotting the mean intensity of all pixels within the region of interest versus the center wavelength of each emission band; this is called the image-guide spectral analysis method.[23] We used this method to record emission spectra of different regions of interest. In this work, all images were 512×512 pixels. The images were obtained at 2.56 μs per pixel.

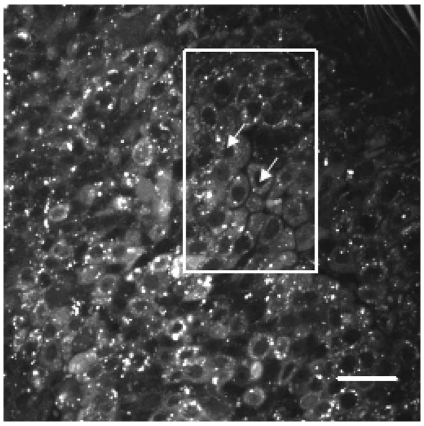

Fig. 1 Image of fluorescent epithelial cells at a depth of 5 μm based on intrinsic TPEF (425 to 618 nm). Excitation wavelength $\lambda_{ex} = 760$ nm and excitation power $P = 2$ mW. Scale bar $= 20$ μm.

2.3 *Statistical Analysis*

Data analysis was performed using Statistical Program for Social Studies for Microsoft Windows (version 13.0). All data are presented as a mean value with its standard deviation indicated (mean+SD) and analyzed using a Student's *t*-test. Differences were considered to be statistically significant when the P values were less than 0.05.

3 Results and Discussion

3.1 *Characterization of Intrinsic TPEF Signals from Respiratory Epithelium*

To characterize the respiratory epithelium, intrinsic TPEF images were obtained. In this work, considering that tissue handling associated with *ex vivo* measurements may deprive tissue of nutrition and that oxygen and the epithelial cells at depth $Z = 0$ μm may be dead, the TPEF images were acquired from depth $Z = 1$ μm into the whole epithelium. Further, taking two-photon action cross sections of reduced pyridine nucleotide (NADH and NADPH) and oxidized flavoproteins (Fp) into account, in the epithelium, we selected 760 nm as the excitation wavelength. At this wavelength, we expect that the observed cellular fluorescence originates primarily from reduced NADH and NADPH and oxidized Fp, while lipides and vitamin D are probably minor contributors.[19] The spectra of NADPH exactly overlay the NADH spectra and the extinction coefficient and quantum yield of both fluorophores is the same, so in this study, they are designated together as NAD(P)H.[24] Shown in Fig. 1 is a representative TPEF image of the respiratory epithelium at depth $Z = 5$ μm. As can be seen in Fig. 1, the epithelial cells can be identified (white arrowheads), showing the fluorescent cytoplasmatic granules of mitochondria, nonfluorescent nuclei displayed darkly on the optical section surrounded by the fluorescent mitochondria, and the clear cellular boundary. In addition, some highly concentrated bright punctate TPEF associated primarily with the bronchial surface was observed. Punctate TPEF has been previously reported in tissue, and its origins are often unknown.[25] Likewise, we were unable to determine the extract origins of these punctate structures, and in this work, we did not analyze this signal. To illustrate additional features

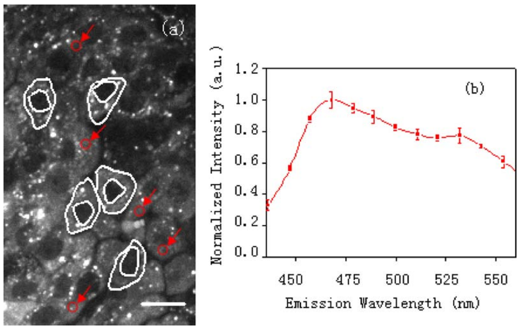

Fig. 2 (a) Magnified image, corresponding to rectangular enclosed region in Fig. 1. (b) Emission spectra obtained from cytoplasmatic mitochondria (red arrowheads). Error bars represent calculated standard deviations ($n=50$ cytoplasmic areas from 10 regions of five samples). Scale bar=10 μm ($\lambda_{ex}=760$ nm, $P=2$ mW). (Color online only.)

with the large-area image, a magnified image from the selected region of interest is shown in Fig. 2(a). In this image, the nuclear-to-cytoplasmic ratio, a parameter related to the developing process of neoplasm, can be quantitatively analyzed. In each cell, the nuclear area is defined as A, and the area of cellular boundary is defined as B. The nuclear-to-cytoplasmic ratio is defined as $A/(B-A)$. In Fig. 2(a), these areas are manually selected from five cells for each region, and the nuclear-to-cytoplasmic ratio is 0.47 ± 0.12 ($n=50$ cells from 10 regions of five samples). In addition, we used the optional HRZ 200 stage to measure the thickness of the respiratory epithelium. Here, the average thickness of respiratory epithelium from 10 regions of five samples is 21 ± 3 μm.

In the following, to determine the cytoplasmic mitochondria signals, the emission spectra from the cytoplasmic regions were acquired using the image-guide spectral analysis method for $\lambda_{ex}=760$ nm. The obtained spectra have been corrected for the wavelength-dependent instrument response, and dark-noise spectra are subtracted from the acquired sample spectra. Each spectrum is normalized to the maximal peak intensity. Figure 2(b) displays a representative spectrum measured from the cytoplasmic region [red arrowheads in Fig. 2(a)] using the image-guide spectral analysis method.[23] As can be seen, there are two peaks at about 470 and 530 nm. It was reported in previous works that the peaks at around 470 and 530 nm possibly result from NAD(P)H and Fp fluorescence, respectively.[14,23,25–27] Specifically, the 470-nm peak corresponds to the NAD(P)H fluorescence, and the 530-nm peak is associated with the presence of Fp. Comparing with single-photon excited fluorescence,[1] the NAD(P)H peak is red-shifted. This may be responsible for the fact that the single- and two-photon fluorescence of NAD(P)H involve different excitation mechanisms. Thus, the intrinsic TPEF of cytoplasmic mitochondria is mainly determined by NAD(P)H and Fp.

Recently, two-photon ratiometric redox fluorometry based on cellular fluorescence from reduced NAD(P)H and oxidized Fp has been proposed as a tool to study mitochondrial energy metabolism.[17,26–28] Specifically, the normalized ratio of these fluorophores [Fp/Fp+NAD(P)H], called the redox ratio, is an indicator of the metabolic state of tissue. Here, the redox ratio was computed on the basis of the NAD(P)H and Fp signals peak intensity using the following equation:

$$Redox_{ratio} = \frac{Fp_{530}}{Fp_{530} + NAD(P)H_{470}}.$$

In this work, in the superficial imaged plane (1 to 5 μm), the redox ratio is 0.42 ± 0.07 ($n=50$ superficial cells from 10 regions of five samples), while in the basal imaged plane (17 to 22 μm), it is 0.38 ± 0.05 ($n=50$ basal cells from 10 regions of five samples). The redox ratio decreases in the basal plane compared with the superficial plane ($n=50$ basal/superficial cell pairs, $P<0.05$), indicating an increase in metabolic activity in the basal cell layer. The result is in agreement with the epithelium physiological process that as the basal cells divide and mature, they move upward through the epithelium, become metabolically less active.[29]

Obviously, intrinsic TPEF signals of the respiratory epithelium can provide a convenient method to demonstrate the changes in the nuclear-to-cytoplasmic ratio, the redox ratio in the epithelium, and the thickness of the epithelium. The epithelium, a cell-rich superficial tissue, is frequently exposed to various forms of physical and chemical damage. Thus, most cancers arise from the epithelium. In the development of epithelial precancer, epithelial cells undergo transformations that give rise to increased nuclear-to-cytoplasmic ratio, decreased redox ratio, and overall thickening of the epithelial layer,[1,21,22] so the demonstration of intrinsic TPEF signals from the respiratory epithelium is of substantial interest.

3.2 *Visualization of the Lamina Reticularis Based on Intrinsic TPEF and SHG Signals*

At about 20 μm deep is the transition zone of the respiratory epithelium and underlying tissue layer. To visualize the transition zone, the TPEF/SHG images were acquired for $\lambda_{ex}=810$ nm, at which no TPEF signal from collagen was detected and the contrast of the TPEF/SHG image can be enhanced.[15] Shown in Fig. 3 are the TPEF/SHG images obtained from the region of attachment between the epithelium and stromal matrix at a depth of 22 μm. As can be seen in Fig. 3(a), there is a mat of large elastic fibers mainly oriented along the longitudinal axis of the airways with cross-linked smaller fibers (white arrowheads). The diameter of the elastic fiber is 1.51 ± 0.31 μm ($n=50$ fibers from 10 regions of five samples). These results are very similar to the *lamina reticularis* images that have been recently obtained from rat trachea using whole mounts of the airways and fluorescence microscopy.[30] According to previous studies,[31] the collagen is supposed to represent the major component of the *lamina reticularis*, but no studies acquired an image of collagen, to the best of our knowledge, within fresh bronchial tissue. This could in part be explained by the fact that at some wavelengths, the fluorescence yield of collagen is at least one order of magnitude smaller than that of elastic fibers.[3] Fortunately, collagen, a noncentrosymmetric molecule, can contribute to an SHG signal.[13,15] Here, we first used SHG signal to image collagen within fresh bronchial tissue. Figure 3(b) shows the SHG image acquired from collagen of the *lamina reticularis*. As can be seen, the distribution and orientation of collagen lamellas are visible. In the following, to better reveal fine details of the microstructural collagen, an additional analysis

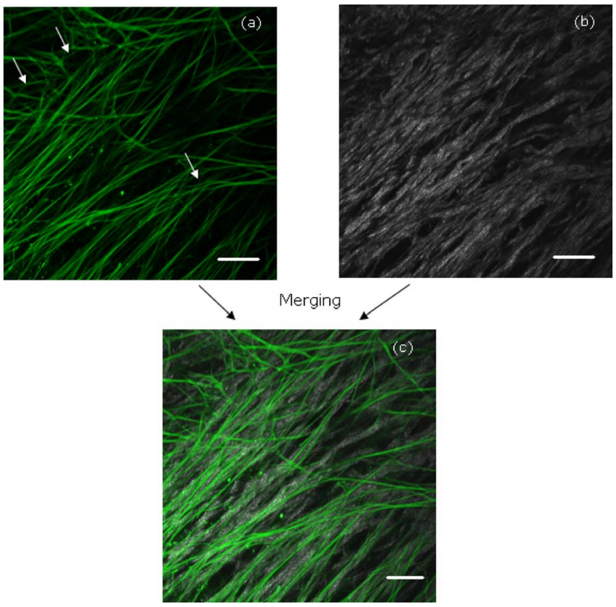

Fig. 3 TPEF/SHG images obtained from the *lamina reticularis* at a depth of 22 μm. The images were acquired by using two independent channels: (a) Typical TPEF image (green color-coded, 447 to 618 nm). (b) SHG image (grayscale color-coded, 398 to 409 nm). (c) TPEF/SHG image obtained by overlaying two channels. Scale bar=20 μm (λ_{ex}=810 nm, $P \leqslant 5$ mW). (Color online only.)

was performed to determine the collagen fibril spacing. In our approach, depicted in Fig. 4, we plotted the SHG intensity profile along selected lines perpendicular to the fibril direction; the fibril count per unit length was determined by counting the number of peaks. Because there is a small intervening space between collagen fibrils and a peak is observed across a fibril, the fibril count per unit length was determined by manually counting the number of peaks. We computed and averaged the collagen fibril spacing over five selected regions of each sample. The averaged collagen fibril spacing is about 0.40 ± 0.13 μm at the *lamina reticularis*.

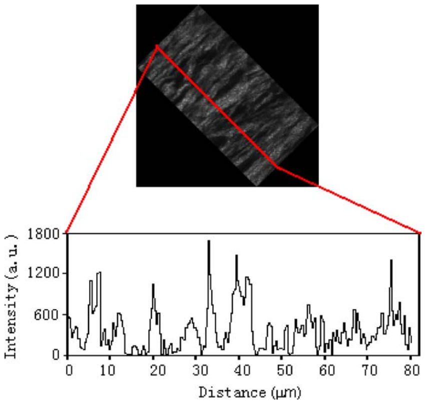

Fig. 4 The collagen fibril counting procedure involves plotting the SHG signal profile along a selected line perpendicular to the fibril orientation. The line in the SHG image of a few collagen fibrils selected in Fig. 3(a) shows an example of such a selection. The profile plot corresponding to that selection is shown below the SHG image.

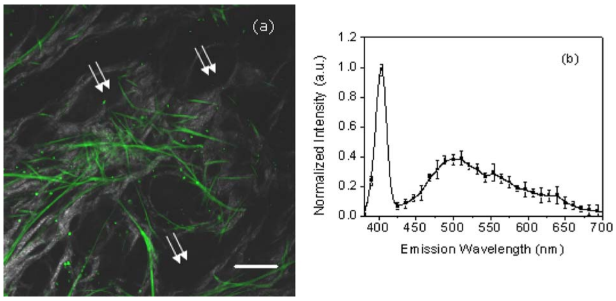

Fig. 5 (a) TPEF/SHG images obtained from stroma at a depth of 40 μm. (b) Emission spectra of stroma. Error bars represent calculated standard deviations (n=10 regions of five samples). Scale bar =20 μm (λ_{ex}=810 nm, $P \leqslant 5$ mW).

Overlaying the TPEF image and SHG image results in high-contrast, high-resolution images that show structural details of the *lamina reticularis*, as shown in Fig. 3(c). The *lamina reticularis* is especially pronounced under the respiratory epithelium of large conducting airways, where it can be several microns thick, which serves as a barrier; binds growth factors, hormones, and ions; and is involved with cellular adhesion, electrical charge, and cell-cell communication.[32–35] Clinically, the *lamina reticularis* is the region of the basement-membrane zone in human large airways that accumulates collagen and leads to the subepithelial fibrosis associated with asthma,[30] so visualization of the *lamina reticularis* based on intrinsic TPEF and SHG signals is very promising.

3.3 *Characterization of Intrinsic TPEF and SHG Signals from Stroma*

Figure 5(a) shows TPEF/SHG images obtained from stroma at a depth of 40 μm. Similar to the *lamina reticularis*, the excitation wavelength is 810 nm. As can be seen, there are two main microstructural components: elastic fibers and collagen fibers. Elastic fibers are the morphology of strings (green color-coded); collagen fibers show a fine mesh of morphology. Interestingly, serous glands were observed in stroma. In Fig. 5(a), some serous glands (indicated by white arrowheads) are surrounded by collagen and display the morphology of a concave polygon (color online only).

To determine the precise origin of image-forming signals from the stromal matrix, the stromal layer spectrum was obtained using the image-guide spectral analysis method for λ_{ex}=810 nm, as shown in Fig. 5(b). The spectrum was accumulated over the entire image of Fig. 5(a). It reveals a sharp peak at 405 nm (exactly half the excitation wavelength) and a broad spectral feature characteristic of TPEF, including three distinct peaks at 500, 554, and 639 nm. The sharp peak at 405 nm has a quadratic dependence on incident laser intensity and shifts with changes in laser frequency to remain at exactly half the excitation wavelength. Collagen is well-known to produce SHG and is responsible for this signal.[13,15] For TPEF signals, the 500-nm peak is associated with the presence of elastic fibers;[14,21–23] the 550-nm peak corresponds to known melanin emission spectra;[14] and the third emission peak at 639 nm may arise from a porphyrin source.[1]

In addition, SHG signals from stroma were observed to decay exponentially with depth (keeping the same excitation

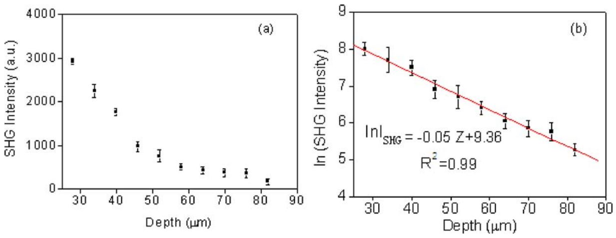

Fig. 6 Dependence of SHG intensity from stromal collagen on penetration depth. (a) Peak values of the SHG spectra versus penetration depth. (b) Plot of the natural logarithm of SHG integrated total intensity versus penetration depth, *Z*, respectively. Error bars represent calculated standard deviations ($n=10$ regions of five samples; $\lambda_{ex}=810$ nm, $P=5$ mW).

power), as shown in Fig. 6(a). In this study, although the pulse width of the excitation pulses could be modulated by scattering and absorption in tissue, the effects are negligible in the range of detection depth (0 to 200 μm) because of the optical sectioning capability and confocal measurement provided by our nonlinear microscopy system. The SHG intensity I decays as a function of depth Z, according to $(I_{SHG})^Z = (I_{SHG})^0 \exp(-AZ)$, where A is an attenuation coefficient that is a function of the sample absorption and scattering properties at both the excitation and emission wavelengths. The inverse of A yields an attenuation length from five samples, $l_{att}=20.0\pm 2.1$ μm, that is a composite optical property of the stroma, as depicted in Fig. 6(b). This finding suggests that the SHG signal's depth-dependent decay can provide a sensitive tool for obtaining quantitative tissue structural information.

Collagen, a source of SHG, is the main scatterer in the stroma underlying the epithelium. The neoplastic progression is associated with regulation of matrix-degrading proteases essential in invasion and metastasis.[36,37] The resulting structural changes in the stromal collagen matrix and possible decomposition of collagen lead to changes in stromal scattering.[38–42] Thus, analysis of the optical property of collagen may be used as an additional diagnostic measure for *in vivo* detection of preinvasive disease.

Recently, it has been recognized that alterations in stromal biology may precede and stimulate neoplastic progression in preinvasive disease,[43,44] so the characterization of intrinsic TPEF and SHG signals from stroma may be of interest for potential mucosal tissue diagnosis.

3.4 *Characterization of Intrinsic TPEF Signals from Hyaline Cartilage*

At deeper sections (above 90 μm), the microstructure exhibits its morphological characteristics different from the microstructure at depth 20 to 90 μm. According to the basic physiology of the bronchus,[2] we know that this layer may be the layer of hyaline cartilage. To visualize the hyaline cartilage, TPEF images were acquired. Figure 7 shows a representative TPEF image of hyaline cartilage at depth $Z=95$ μm. Similar to the case of the epithelium, the excitation wavelength is 760 nm. As can be seen, chondrocytes are situated far apart in fluid-filled spaces, and the lacunae can be identified through the fluorescent cytoplasm and dark nonfluorescent nuclei (white arrowheads). In addition, cellular matrix structures can be clearly displayed based on strongly intrinsic TPEF. Similar to respiratory epithelium, in Fig. 8(a), the nuclear-to-cytoplasmic ratio of chondrocytes is 0.65 ± 0.17 μm ($n=50$ cells from 10 regions of five samples).

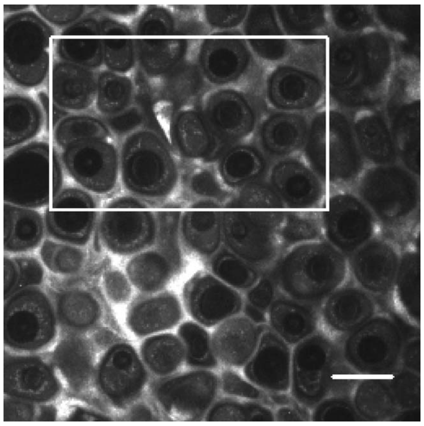

Fig. 7 Intrinsic TPEF (425 to 618 nm) imaging of hyaline cartilage. Scale bar=20 μm($\lambda_{ex}=760$ nm$P=6$ mW).

To determine the precise origin of image-forming signals from hyaline cartilage, the emission spectra from the cytoplasmic and extracellular matrix regions were acquired using the image-guide spectral analysis method for $\lambda_{ex}=760$ nm. Figure 8(b) displays representative spectra measured from the cytoplasmic region [red arrowheads in Fig. 8(a)] and from the extracellular matrix [green arrowheads in Fig. 8(a)] using the image-guide spectral analysis method. As can be seen, there are two peaks at about 470 and 530 nm in the cytoplasmic region. The peaks at around 470 and 530 nm possibly result

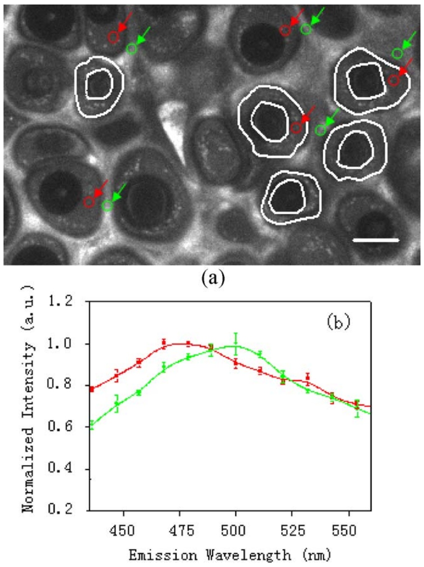

Fig. 8 (a) Magnified image (corresponding to the rectangular enclosed region in Fig. 7). (b) Emission spectra obtained from cytoplasmatic mitochondria (red arrowheads) and from matrix (green arrowheads). Error bars represent calculated standard deviations ($n=50$ cytoplasmic/matrix areas from 10 regions of five samples). Scale bar $=10$ μm ($\lambda_{ex}=760$ nm, $P=6$ mW). (Color online only.)

from NAD(P)H and Fp fluorescence, respectively. Similar to the respiratory epithelium, the redox ratio can be also measured and is 0.46 ± 0.11 ($n=50$ cytoplasmic areas from 10 regions of five samples). In the extracellular matrix, a 500-nm peak, associated with collagen and noncollagenous pericellular matrix, was observed.

Hyaline cartilage has many functions in physiology, such as reducing friction at joints, controlling the longitudinal growth of bone, and maintaining of the normal bronchial wall tissue architecture.[45,46] Thus, the demonstration of intrinsic TPEF signals from hyaline cartilage may provide a valuable tool to study these physiological processes.

4 Conclusion

In this study, we demonstrated the use of NLOM for imaging the mouse bronchial wall microstructure. Intrinsic nonlinear optical signals obtained from the bronchus were shown to provide excellent microstructural and biochemical characterization of the bronchial tissue.

Our results show that NLOM allows quantitative imaging of particular tissue constituents with subcellular resolution and without need for sectioning. It can offer a ratiometric redox fluorometry based on TPEF from cellular NAD(P)H and Fp to study mitochondrial energy metabolism and a model based on the exponential depth-dependent decay of the reflected SHG intensity for obtaining quantitative information on the optical property of the stroma that can be potentially be used for the characterization of normal and diseased tissue states.

To the best of our knowledge, this is the first report on imaging the bronchial wall microstructure with high spatial resolution and high contrast without labeling or slicing based on intrinsic nonlinear optical contrast. This study shows the potential of NLOM as a powerful noninvasive technique to characterize bronchial physiology and pathology. With the advent of nonlinear optical endoscopy, we foresee potential applications of the NLOM technique to *in vivo* real-time assessment of bronchial disease in the future.

Acknowledgments

The project was supported by the National Natural Science Foundation of China (No. 60508017, 60678054), the Natural Science Foundation of Fujian Province of China (2007J0007 and C0720001) and the Science and Technology Planning Key Program of Fujian Province (2008Y0037) and Program for New Century Excellent Talents in University (NCET-07-0191).

References

1. R. R. Richards-Kortum and E. Sevick-Muraca, "Quantitative optical spectroscopy for tissue diagnosis," *Annu. Rev. Phys. Chem.* **47**, 555–606 (1996).
2. S. C. Whiteman, Y. Yang, D. G. Pittius, M. Stephens, J. Parmer, and M. A. Spiteri, "Optical coherence tomography: real-time imaging of bronchial airways microstructure and detection of inflammatory/neoplastic morphologic changes," *Clin. Cancer Res.* **13**, 813–818 (2006).
3. L. Thiberville, S. Moreno-Swirc, T. Vercauteren, E. Peltier, C. Cave, and G. B. Heckly, "*In vivo* imaging of the bronchial wall microstructure using fibered confocal fluorescence microscopy," *Am. J. Respir. Crit. Care Med.* **175**, 22–31 (2007).
4. D. J. Stechschulte, J. J. Wu, and D. R. Eyre, "Fibronectin lacking the ED-B domain is a major structural component of tracheal cartilage," *J. Biol. Chem.* **272**, 4783–4786 (1997).
5. T. J. Shaw, S. Wakely, C. R. Peebles, R. L. Mehta, J. M. Turner, S. J. Wilson, and P. H. Howarth, "Endobronchial ultrasound to assess airway wall thickening: validation *in vitro* and *in vivo*," *Eur. Respir. J.* **23**, 813–817 (2004).
6. H. Tashita, R. Inoue, E. Goto, and N. Kondo, "Magnetic resonance imaging for early detection of bronchial foreign bodies," *Eur. J. Pediatr.* **157**, 442–443 (1998).
7. T. Kennedy, S. Lam, and F. Hirsch, "Review of recent advances in fluorescence bronchoscopy in early localization of central airway lung cancer," *Oncologist* **6**, 257–262 (2001).
8. P. T. C. So, Y. D. Chen, and R. M. Barry, "Two-photon excitation fluorescence microscopy," *Annu. Rev. Biomed. Eng.* **2** 399–429 (2000).
9. W. R. Zipfel, R. M. Williams, and W. W. Webb, "Nonlinear magic: multiphoton microscopy in the biosciences," *Nat. Biotechnol.* **21**, 1369–1377 (2003).
10. L. Fu, A. Jain, C. Cranfield, H. K. Xie, and M. Gu, "Three-dimensional nonlinear optical endoscopy," *J. Biomed. Opt.* **12**, 040501-1-3 (2007).
11. B. A. Flusberg, J. C. Jung, E. D. Cocker, E. P. Anderson, and M. J. Schnitzer, "*In vivo* brain imaging using a portable 3.9-gram two-photon fluorescence microendoscope," *Opt. Lett.* **30**, 2272–2274 (2005).
12. K. König, "Clinical two-photon microendoscopy," *Microsc. Res. Tech.* **70**, 398–402 (2007).
13. P. J. Campagnola, and L. M. Loew, "Second-harmonic imaging microscopy for visualizing biomolecular arrays in cells, tissues, and organisms," *Nat. Biotechnol.* **21**, 1356–1360 (2003).
14. L. H. Laiho, S. Plete, T. M. Hancewicz, P. D. Kaplan, and P. T. C. So, "Two-photon 3-D mapping of *ex vivo* human skin endogenous fluorescence species based on fluorescence emission spectra," *J. Biomed. Opt.* **10**, 0240161–10 (2005).
15. A. Zoumi, A. Yeh, and B. J. Tromberg, "Imaging cells and extracellular matrix *in vivo* by using second-harmonic generation and two-photon excited fluorescence," *Proc. Natl. Acad. Sci. U.S.A.* **99**, 11014–11019 (2002).
16. M. J. Koehler, K. Koenig, P. Elsner, R. Buckle, and M. Kaatz, "*In vivo* assessment of human skin aging by multiphoton laser scanning tomography," *Opt. Lett.* **31**, 2879–2881 (2006).
17. J. G. Lyubovitsky, J. A. Spencer, T. B. Krasieva, B. Andersen, and B. J. Tromberg, "Imaging corneal pathology in a transgenic mouse model using nonlinear microscopy," *J. Biomed. Opt.* **11**, 0140131–6 (2006).
18. S. J. Lin, R. J. Wu, H. Y. Tan, W. Lo, W. C. Lin, T. H. Young, C. J. Hsu, J. S. Chen, S. H. Jee, and C. Y. Dong, "Evaluating cutaneous photoaging by use of multiphoton fluorescence and second-harmonic generation microscopy," *Opt. Lett.* **17**, 2275–2277 (2005).
19. W. R. Zipfel, R. M. Williams, R. Christie, A. Y. Nikitin, B. T. Hyman, and W. W. Webb, "Live tissue intrinsic emission microscopy using multiphoton-excited native fluorescence and second harmonic generation," *Proc. Natl. Acad. Sci. U.S.A.* **100**, 7075–7080 (2003).
20. E. Brown, T. McKee, E. diTomaso, A. Pluen, B. Seed, Y. Boucher, and R. K. Jain, "Dynamic imaging of collagen and its modulation in tumors *in vivo* using second-harmonic generation," *Nat. Med.* **9**, 796–800 (2003).
21. S. M. Zhuo, J. X. Chen, X. S. Jiang, S. S. Xie, R. Chen, N. Cao, Q. L. Zou, and S. Y. Xiong, "The layered-resolved microstructure and spectroscopy of mouse oral mucosa using multiphoton microscopy," *Phys. Med. Biol.* **52**, 4967–4980 (2007).
22. J. X. Chen, S. M. Zhuo, R. Chen, X. S. Jiang, S. S. Xie, and Q. L. Zou, "Depth-resolved spectral imaging of rabbit esophageal tissue based on two-photon excited fluorescence and second-harmonic generation," *New. J. Phys.* **9**, 212(1–12) (2007).
23. S. M. Zhuo, J. X. Chen, T. S. Luo, D. S. Zuo, and J. J. Zou, "Multimode nonlinear optical imaging of the dermis in *ex vivo* human skin based on the combination of multichannel mode and Lambda mode," *Opt. Express* **14**, 7810–7820 (2006).
24. G. H. Patterson, S. M. Knobel, P. Arkhammar, O. Thastrup, and D. W. Piston, "Separation of the glucose-stimulated cytoplasmic and mitochondrial NAD(P)H responses in pancreatic islet β cells," *Proc. Natl. Acad. Sci. U.S.A.* **97**, 5203–5207 (2000).
25. P. Kloppenburg, W. R. Zipfel, W. W. Webb, and R. M. Harris-Warrick, "Highly localized Ca(2+) accumulation revealed by multi-

photon microscopy in an identified motoneuron and its modulation by dopamine," *J. Neurosci.* **20**, 2523–2533 (2000).

26. S. Huang, A. A. Heikal, and W. W. Webb, "Two-photon fluorescence spectroscopy and microscopy of NAD(P)H and flavoprotein," *Biophys. J.* **82**, 2811–2825 (2002).
27. L. M. Tiede, S. M. Rocha-Sanchez, R. Hallworth, M. G. Nichols, and K. Beisel, "Determination of hair cell metabolic state in isolated cochlear preparations by two-photon microscopy," *J. Biomed. Opt.* **12**, 0210041-8 (2007).
28. B. Chance, P. Cohen, F. Jobsis, and B. Schoener, "Intracellular oxidation-reduction states *in vivo*," *Science* **137**, 499–508 (1962).
29. B. Alberts, A. Johnson, J. Lewis, M. Raff, K. Roberts, and P. Walter, *Molecular Biology of the Cell*, Garland Science, New York (2002).
30. M. Evans, W. L. Van, M. Fanucchi, E. Toskala, E. Luck, P. Sannes, and G. Plopper, "Three-dimensional organization of the *lamina reticularis* in the rat tracheal basement membrane zone," *Am. J. Respir. Cell Mol. Biol.* **22**, 393–397 (2000).
31. J. M. Ray and W. G. Stetler-Stevenson, "The role of matrix metalloproteases and their inhibitors in tumour invasion, metastasis and angiogenesis," *Eur. Respir. J.* **7**, 2062–2072 (1994).
32. E. Adachi, I. Hopkinson, and T. Hayashi, "Basement-membrane stromal relationships: interactions between collagen fibrils and the *lamina densa*," *Int. Rev. Cytol.* **173**, 73–156 (1997).
33. S. E. Dunsmore and D. E. Rannels, "Extracellular matrix biology in the lung," *Am. J. Physiol.* **270**, L3–L27 (1996).
34. H. J. Merker, "Morphology of the basement membrane," *Microsc. Res. Tech.* **28**, 95–124 (1994).
35. P. L. Sannes and J. Wang, "Basement membranes and pulmonary development," *Exp. Lung Res.* **23**, 101–108 (1997).
36. M. M. Mueller and N. E. Fusenig, "Tumor-stroma interactions directing phenotype and progression of epithelial skin tumor cells," *Differentiation* **70**, 486–497 (2002).
37. P. Zigrino, S. Loffek, and C. Mauch, "Tumor-stroma interactions: their role in the control of tumor cell invasion," *Biochimie* **87**, 321–328 (2005).
38. K. J. Heppner, L. M. Matrisian, R. A. Jensen, and W. H. Rodgers, "Expression of most matrix metalloproteinase family members in breast cancer represents a tumor-induced host response," *Am. J. Pathol.* **149**, 273–282 (1996).
39. I. Pavlova, K. Sokolov, R. Drezek, A. Malpica, M. Follen, and R. Richards-Kortum, "Microanatomical and biochemical origins of normal and precancerous cervical autofluorescence using laser-scanning fluorescence confocal microscopy," *Photochem. Photobiol.* **77**, 550–555 (2003).
40. P. Wilder-Smith, K. Osann, N. Hanna, N. El Abbadi, M. Brenner, D. Messadi, and T. Krasieva, "*In vivo* multiphoton fluorescence imaging: a novel approach to oral malignancy," *Lasers Surg. Med.* **35**, 96–103 (2004).
41. I. Georgakoudi, E. E. Sheets, M. G. Muller, V. Backman, C. P. Crum, K. Badizadegan, R. R. Dasari, and M. S. Feld, "Trimodal spectroscopy for the detection and characterization of cervical precancers *in vivo*," *Am. J. Obstet. Gynecol.* **186**, 374–382 (2002).
42. M. G. Muller, T. A. Valdez, I. Georgakoudi, V. Backman, C. Fuentes, S. Kabani, N. Laver, Z. Wang, C. W. Boone, R. R. Dasari, S. M. Shapshay, and M. S. Feld, "Spectroscopic detection and evaluation of morphologic and biochemical changes in early human oral carcinoma," *Cancer* **97**, 1681–1692 (2003).
43. W. K. Hong and M. B. Sporn, "Recent advances in chemoprevention of cancer," *Science* **278**, 1073–1077 (1997).
44. T. Bogenrieder and M. Herlyn, "Axis of evil: molecular mechanisms of cancer metastasis," *Oncogene* **22**, 6524–6536 (2003).
45. S. A. Yousem, J. H. Dauber, and B. P. Griffith, "Bronchial cartilage alterations in lung transplantation," *Chest* **98**, 1121–1124 (1990).
46. Q. Tan, R. Steiner, S. P. Hoerstrup, and W. Weder, "Tissue-engineered trachea: history, problems and the future," *Eur. J. Cardiothorac Surg.* **30**, 782–786 (2006).